AMERICAN METEOROLOGICAL SOCIETY

Journal of Climate

EARLY ONLINE RELEASE

The DOI for this manuscript is doi: 10.1175/JCLI-D-12-00113.1

Precursor Signals and Processes Associated with MJO Initiation over the Tropical Indian Ocean

Chongbo Zhao[1, 2], Tim Li[3], Tianjun Zhou[1]

1 LASG, Institute of Atmospheric Physics, Chinese Academy of Sciences, China

2 Graduate University of Chinese Academy of Sciences, China

3 IPRC and Department of Meteorology, University of Hawaii, 2525 Correa Rd., Honolulu, HI 96822, USA

Submitted to J. Climate in Feb. 2012

Revised on Jun. 15, 2012

Corresponding author: Tim Li, IPRC and Department of Meteorology, University of Hawaii, Honolulu, Hawaii

Abstract

The precursor signals of convection initiation associated with the Madden-Julian Oscillation (MJO) in boreal winter were investigated through the diagnosis of the ERA-40 reanalysis for the period of 1982-2001. The western equatorial Indian Ocean (WIO) is a key region of the MJO initiation. A marked increase of specific humidity and temperature in the lower troposphere appears 5-10 days prior to the convection initiation. The increased moisture and temperature causes a convectively more unstable stratification, leading to the onset of convection.

A diagnosis of lower-tropospheric moisture (heat) budgets shows that the moisture (temperature) increase is caused primarily by the horizontal advection of the mean specific humidity (temperature) by the MJO flow. The anomalous flow is primarily determined by the downstream Rossby wave response to a preceding suppressed-phase MJO over the eastern Indian Ocean, whereas the upstream Kevin wave response to the previous eastward-propagating convective-phase MJO is not critical. An idealized numerical experiment further supports this claim.

The Southern Hemisphere (SH) mid-latitude Rossby wave train and associated wave activity flux prior to the MJO initiation were diagnosed. It is found that SH mid-latitude Rossby waves may contribute to MJO initiation over the western Indian Ocean through wave energy accumulation. Idealized numerical experiments confirm that SH mid-latitude perturbations play an important role in affecting the MJO variance in the tropics. A barotropic energy conversion diagnosis indicates that there is continuous energy transfer from the mean flow to intraseasonal disturbances over the initiation region, which may help trigger MJO development.

1. Introduction

The tropical intraseasonal oscillation (ISO), also called Madden–Julian oscillation (MJO), is one of dominant atmospheric low-frequency modes in the tropics. It is characterized by the eastward propagation of large-scale convection and zonal wind along the equator in boreal winter, with a typical 20-90-day periodicity and a planetary zonal scale (Madden and Julian 1971, 1972, 1994; Li and Zhou 2009). An unsolved question regarding its life cycle is how MJO is initiated over the western equatorial Indian Ocean (WIO).

A number of theories have been advanced in understanding the initiation of the MJO. These theories may be classified according to an internal (tropical) or an external (extratropical) origin. The tropical origin hypotheses include the forcing from upstream (i.e., west of the initiation region) related to a previous MJO event that circumnavigates around the global tropics (e.g., Lau and Peng 1987; Wang and Li 1994; Matthews 2000, 2008; Seo and Kim 2003) and processes due to local changes in air-sea fluxes and underlying SST (e.g., Li et al. 2008), planetary boundary layer (PBL) moisture and convergence (Kemball-Cook and Weare 2001; Jiang and Li 2005), or cloud-radiation-moisture feedbacks (Bladé and Hartmann 1993; Hu and Randall 1994; Raymond 2000; Sobel and Gildor 2003; Zhang and Song 2009; Maloney et al. 2010). The promise behind the circumnavigating theory is that the eastward-propagating MJO wave may trigger deep convection over moist and warm Indian Ocean after it passes the African continent, with possible topographic lifting effect (Hsu and Lee 2005). In this scenario, the forcing from the upstream (west of the initiation region) holds a key for triggering new convection over the WIO. Different from this upstream forcing scenario, Jiang and Li (2005) proposed a downstream forcing scenario, in which a negative MJO heating over the eastern equatorial Indian Ocean (EIO) may initiate an opposite-phase MJO in the WIO. The change of the PBL moisture was attributed to

anomalous ascending (or descending) motion induced by temperature advection. Bladé and Hartmann (1993) and Hu and Randall (1994) suggested that the initiation of convection in the tropical Indian Ocean is a result of self-adjustment of a stationary heat source by nonlinear interactions among radiation, convection and surface moisture flux between active and inactive convection regimes. Li et al. (2008) suggested that cold SST anomalies induced by an eastward-propagating active-phase MJO may exert a delayed feedback to the subsequent, opposite-phase MJO.

The extratropical origin hypotheses emphasized forcing from mid-latitude perturbations including the energy dispersion or the momentum transport of mid-latitude Rossby waves and mid-latitude baroclinic eddies (e.g., Hsu et al. 1990; Bladé and Hartmann 1993; Matthews and Kiladis 1999; Slingo et al. 1999; Lin et al. 2000; Pan and Li 2007; Lin et al. 2007; Ray et al. 2009). For example, Hsu et al. (1990) suggested a triggering effect by extratropical perturbations on tropical convection based on a case study. Kiladis and Weickmann (1992) showed that the extratropical Rossby wave trains propagating into the Tropics from mid-latitude played a role in organizing MJO convection.

Most of the studies above were based on either a theoretical model with simplified dynamic framework or a case study. The present study is aimed to reveal precursor signals and processes associated with MJO initiation based on the diagnosis of 20-year observational and reanalysis data. From a microscopic view, we will examine the local moisture and heat budgets to reveal specific processes that give rise to the convection initiation over the WIO. From a macroscopic view, we will further investigate the relative importance of upstream versus downstream processes and extratropical versus tropical forcing effects. The rest of this paper is organized as follows. The datasets and methods employed in this study are presented in section 2. In section 3,

we reveal the precursor dynamic and thermodynamic signals of the MJO initiation. Then a lower-tropospheric moisture and heat budget analysis is followed in sections 4. In section 5, the upstream and downstream forcing effect is further examined. In section 6, we investigate possible mid-latitude impacts through the diagnosis of wave activity flux convergence and idealized numerical experiments. Finally, the conclusion and discussion are given in the last section.

2. Data, methods and numerical experiments

a. Data

The primary datasets used for this study are the National Oceanic and Atmospheric Administration (NOAA) outgoing longwave radiation (OLR; Liebmann and Smith 1996) and the European Centre for Medium-Range Weather Forecast (ECMWF) Re-Analysis (ERA-40; Uppala et al. 2005). All the datasets have a horizontal resolution of 2.5° ×2.5°. The OLR is used as a proxy for deep convection in the tropics. The ERA-40 reanalysis data include multiple-level horizontal velocity, vertical velocity, specific humidity, temperature and geopotential height. In this study, we focus on the MJO behavior in northern winter (November - April) for the period of 1982-2001.

b. Analysis methods

An EOF analysis was employed to extract the dominant modes of MJO convection. Before performing the EOF analysis, daily OLR and other atmospheric variables including 3D wind, geopotential height, specific humidity and temperature during 1982-2001 were subject to a 20-90-day band-pass filtering based on harmonic decomposition (Kemball-Cook and Wang 2001;

Teng and Wang 2003; Jiang et al. 2004). The filtered OLR data from November to April each year were then used for the EOF analysis. The domain for the EOF analysis spans from 30°S to 30°N and from 40°E to 180°E. The corresponding atmospheric wind, humidity and temperature patterns are derived based on the composite analysis of time series of the dominant EOF mode.

To understand the moisture and temperature changes associated with MJO initiation, both the moisture and heat budgets were calculated. According to Yanai et al. (1973), the temperature tendency at each constant pressure level is determined by the sum of horizontal temperature advection, adiabatic process associated with vertical motion, and the atmospheric apparent heat source, Q_1. The moisture tendency at each constant pressure level is determined by the sum of horizontal and vertical moisture advection and the atmospheric apparent moisture sink, Q_2. The temperature and moisture tendency equations may be written as

$$\frac{\partial T}{\partial \mathrm{t}} = -V\nabla T + \omega\frac{RT}{c_p p} - \omega\frac{\partial T}{\partial \mathrm{p}} + Q_1 / c_p \qquad (1)$$

$$\frac{\partial q}{\partial \mathrm{t}} = -V\nabla q - \omega\frac{\partial q}{\partial \mathrm{p}} - \frac{Q_2}{L} \qquad (2)$$

where c_p denotes the specific heat at constant pressure, R the gas constant, ∇ the horizontal gradient operator, L the latent heat of condensation, t time, p pressure, T temperature, q specific humidity, V horizontal velocity vector, and ω vertical p-velocity. $(RT/c_p p)$ - $(\partial T/\partial \mathrm{p})$ represents the static stability. Note that Q_1 represents the total diabatic heating including radiation, latent heating, surface heat flux, and subgrid-scale processes; Q_2 represents the latent heating due to condensational or evaporational processes in the atmosphere and subgrid-scale moisture flux convergence (Yanai et al. 1973). Applying a 20-90-day band-pass filtering operator to the equations above and integrating each term vertically from the surface (1000hPa) to 700 hPa, one may derive the intraseasonal low-tropospheric moisture and heat budget equations.

c. Numerical experiments

The atmospheric general circulation model (AGCM) used in the study is ECHAM version 4.6 (hereafter ECHAM4), which was developed by the Max Planck Institute for Meteorology (MPI; Roeckner et al. 1996). The model was run at a horizontal resolution of spectral triangular 42 (T42), roughly equivalent to 2.8 latitude×2.8 longitude, with 19 vertical levels in a hybrid sigma-pressure coordinate system extending from surface to 10 hPa. ECHAM4 is one of the best AGCMs in the simulation of MJO (Lin et al. 2006), and it has been used in studying the role of air-sea interaction on MJO (Fu et al. 2002), northward propagation of boreal summer ISO (Jiang et al. 2004) and MJO predictability (Fu et al. 2009).

To identify the relative contributions of the circumnavigating MJO mode and the mid-latitude forcing effect in triggering MJO convection, we design a set of sensitivity experiments. In the control experiment, the model is forced by the climatological monthly SST. In the first sensitivity experiment (termed as "EXP_TA"), a strong Newtonian-type damping is applied to force the model prognostic variables (such as u, v, q, T) toward the model climatologic annual cycle retrieved from the control run over the tropical Atlantic (20°S-20°N, 60°W-20°E) region. By doing so, the mean state over the tropical Atlantic region remains the same while intraseasonal and higher-frequency variability is greatly suppressed. Through this experiment, we intentionally suppress the circumnavigating MJO mode. The difference of the MJO variance between the control run and EXP_TA may reflect how strong the effect of the upstream forcing is on the MJO initiation.

In the second sensitivity experiment (termed as "EXP_NS"), similar Newtonian damping is applied over two latitudinal zones, 20°S-30°S and 20°N-30°N, to force the model prognostic variables toward the controlled climatologic annual cycle. By doing so, the intraseasonal and higher-frequency variability over the transitional zones is greatly suppressed and tropics-midlatitude connection is broken. As a result, the mid-latitude influence on the tropical MJO variability is intentionally suppressed. The difference between the control and the EXP_NS run illustrates how strong the effect of the mid-latitude forcing is on the MJO variability.

To distinguish the Southern Hemisphere (SH) and Northern Hemisphere (NH) forcing effect, the sensitivity experiments (termed as "EXP_SH" and "EXP_NH") were conducted. In EXP_SH (EXP_NH) run, the same Newtonian damping approach was only applied to the SH (NH) latitudinal zone, 20°S-30°S (20°N-30°N). By doing so, the SH (NH) mid-latitude influence on the tropical MJO variability is suppressed. The differences between the EXP_SH run and the EXP_NH run illustrate the relative contribution of the SH and NH mid-latitude forcing on the tropical MJO variability. Table 1 lists all these numerical experiments.

3. Dynamic and thermodynamic precursor signals prior to MJO initiation

Many previous studies identified MJO signals using a linear principal component analysis in a global tropics domain (e.g., Maloney and Hartmann 1998; Kessler 2001; Wheeler and Hendon 2004). To clearly identify processes associated with MJO initiation, a regional EOF analysis was employed over the Indo-Pacific warm pool region. The EOF analysis of the intraseasonal OLR anomaly reveals two dominant patterns in northern winter (Fig. 1a, b). The first EOF mode accounts for about 12% of the total variance. The most conspicuous feature of this mode is a seesaw in convection over the tropical Indian Ocean and the tropical western

Pacific. The second EOF mode (Fig. 1b) explains about 10% of the total variance. This mode shows a suppressed convection center over the Maritime Continent. Figure 1c shows that the time series of the two leading EOF modes are significantly correlated. Thus, the two modes reflect the eastward propagating MJO mode at different phases. The maximum positive correlation occurs around -10 day, implying that the second mode leads the first mode by 10 days.

The time series of the first EOF mode was used to select strong MJO events for the subsequent composite analysis. Here the strong MJO events are identified by the amplitude of the first principal component exceeding one standard deviation, as indicated by the horizontal dashed lines in Fig. 1d. During the 20-yr period, 55 cases with strong negative OLR center located over the EIO were selected. On the average, it is about 3 MJO cases each winter. Composite OLR evolution patterns were derived based on the 55 events, with a reference day (day 0) corresponding to each peak above the one standard deviation line in Fig. 1d. Thus, day 0 represents the time when an enhanced MJO convection center appears over the EIO.

To reveal the key initiation region in the Indian Ocean, we examine both the maximum ISO variance map and the composite OLR evolution map. Figure 2 shows the maximum OLR variance pattern associated with MJO in northern winter. It is clear that the maximum variability of MJO convective activity in the WIO appears south of the equator. This is understandable because the seasonal mean convection is also located south of the equator in boreal winter (e.g., Hsu and Li 2012). Figure 3 illustrates the composite evolution of OLR from day -9 to day 0 at a 3-day interval. The composite OLR at day 0 resembles the first EOF mode pattern, as expected. The OLR evolution maps reveal that the MJO convection was firstly initiated in the southwestern

Indian Ocean, and then it propagates eastward. During its eastward journey, the convection is strengthened and shifts more toward the equator.

Based on the MJO variance and evolution maps, the region of (20°S-0°N, 50°E-70°E) is defined as the MJO convection initiation region. To reveal precursor signals associated with the convection initiation, we examine the time evolution of several key atmospheric variables averaged over the region. Figure 4a presents the time evolution of the intraseasonal OLR anomaly averaged over (20°S-0°N, 50°E-70°E). Note that the OLR anomaly transitions from a positive to a negative value at day -15. Consistent with the OLR transition is the switch of sign of the mid-tropospheric vertical motion, from an anomalous descending motion to an anomalous ascending motion (Fig. 4b). Thus day -15 is regarded as the initiation date.

It is interesting to note that 5-10 days prior to the initiation date, a marked sign change of the specific humidity and temperature fields appears in the lower troposphere (Fig. 4c and d), that is, the lower-tropospheric specific humidity and temperature anomalies transition from a negative value to a positive value one week prior to the initiation date. The specific humidity perturbation is initially confined at low level and gradually penetrates into the middle troposphere. At day -15, the positive moisture anomaly has extended up to 500 hPa. The temperature perturbation, on the other hand, is primarily confined below 700 hPa till day -8.

The marked increase of both the lower-tropospheric specific humidity and temperature leads to an increase of equivalent potential temperature (θ_e) and moist static energy (MSE) in the lower troposphere, as shown in Fig. 4e and f. The vertical time cross section of θ_e shows that about one week prior to the initiation date, a positive θ_e perturbation appears in the lower troposphere. This positive perturbation intensifies rapidly while extending upward, closely following the specific humidity evolution.

Considering the wide range of temporal spectrum of the MJO signal, we conducted a sensitivity test by making MJO composite analysis based on phase, not lagged day. Each of individual MJO events was separated into 13 phases (on average 4 days per phase) from 0° to 360° at an interval of 30°. A similar low-tropospheric moisture and temperature precursor signal is found about 8 days prior to convection initiation (figure not shown). Thus the phase composite result is consistent with the lagged-day composite result.

The greater increase of low-level θ_e may potentially lead to a convectively more unstable stratification. We introduced a potential instability parameter that is defined as the difference of equivalent potential temperature between the lower troposphere (1000-700 hPa) and the mid-troposphere (400-300 hPa):

$$\Delta\theta_e = \theta_{eL|1000\text{-}700hPa} - \theta_{eM|400\text{-}300hPa} \qquad (3)$$

where θ_{eL} denotes the averaged θ_e over 700-1000 hPa, θ_{eM} represents the averaged θ_e over 300-400 hPa. A positive (negative) $\Delta\theta_e$ implies that the atmosphere is more (less) convectively unstable. The time evolution of $\Delta\theta_e$ shows that the instability parameter increases rapidly from day -25 to day -15 (Fig. 5a). The marked increase is primarily attributed to the increase of lower-tropospheric equivalent potential temperature, while the equivalent potential temperature in the mid-troposphere does not change much during the period. This implies that the increase of the lower-tropospheric moisture and temperature preconditions a convectively more unstable stratification, which eventually leads to the initiation of the MJO convection.

Next we examine what processes contribute to the increase of low-level moisture and temperature prior to the initiation date. As shown in Fig. 4, both the moistening and warming in the lower troposphere occur one week prior to the initiation date. Such the moistening and warming may build up local moist static energy and favor for the generation of new convection.

To quantitatively measure the relative contribution of the moistening and warming to the $\Delta\theta_e$ increase from day -25 to day -15, we conducted the following two calculations. Firstly we kept the specific humidity constant on the intraseasonal timescale while allowing the temperature to change realistically. Secondly we kept the temperature constant while allowing the humidity to vary. The result shows that the specific humidity change plays a more important role, and it contributes to about 75% of the $\Delta\theta_e$ change (Fig. 5b). This points out that the preconditioning of moisture is crucial for MJO convection initiation, whereas the increase of lower-tropospheric temperature also plays a role.

4. Moisture and heat budget diagnoses

The analysis above indicates that lower-tropospheric moistening and warming prior to the convection initiation is crucial for the establishment of a convectively more unstable stratification. What physical processes contribute to the lower-tropospheric moistening and warming? In this section, both the lower-tropospheric moisture and heat budgets are diagnosed, in order to address this question.

Figure 6 shows the diagnosis result from vertically-integrated (from 1000 hPa to 700 hPa) intraseasonal moisture budget terms. It is clear that the positive moisture tendency during the initiation period (from day -25 to -15) is mainly attributed to the horizontal advection, while the vertical advection (due to subsidence and associated divergence) is against the lower-tropospheric moistening. The result indicates that the lower-tropospheric moistening process during the MJO initiation is very different from that during the MJO eastward propagation phase. In the latter case the lower-tropospheric moistening is primarily attributed to the vertical advection associated with PBL convergence (Hsu and Li 2012).

The apparent moisture source term ($-Q_2/L$) plays a minor but positive role in the low-tropospheric moistening. This is because anomalous descending motion during the initiation period reduces the mean precipitation, leading to less condensational heating and thus more moisture retained in the atmosphere. The surface latent heat flux anomaly, on the other hand, does not contribute to the moistening during the initiation period (Fig. 6c).

To examine specific horizontal advection processes that contribute to the lower-tropospheric moistening, both the specific humidity and wind fields are decomposed into three components, the low-frequency background state (LFBS, with a period longer than 90 days), the intraseasonal (20-90-day) component, and the high-frequency (with a period less than 20 days) component:

$$q=\bar{q}+q'+q^*,\quad u=\bar{u}+u'+u^*,\quad v=\bar{v}+v'+v^* \qquad (4$$

where a bar, a prime and a star denote the LFBS, MJO and high-frequency component respectively.

Figure 6b shows the contributions from each of nine horizontal advection terms. The largest term comes from the advection of the mean moisture by the MJO flow ($-\mathbf{V}'\cdot\nabla\bar{q}$). The second largest term is the advection of anomalous moisture by the LFBS flow ($-\bar{\mathbf{V}}\cdot\nabla q'$).

Figure 7a presents the horizontal patterns of the LFBS specific humidity field and the MJO wind perturbation field. Both the background specific humidity and anomalous wind fields were derived based on the time average from day -25 to day -15 and vertical integration from 1000 hPa to 700 hPa. The maximum LFBS specific humidity is located along 10°S, where the seasonal mean convection is also strongest. Note that the MJO flow during the initiation period is dominated by anomalous easterlies and two anticyclonic Rossby gyres over the tropical Indian

Ocean. Such a wind anomaly resembles the Gill (1980) pattern and is typically observed when the suppressed MJO convection is located in the EIO. A further examination of the intraseasonal OLR field confirms that a maximum positive OLR center associated with MJO is indeed located over the EIO during the period (Fig. 11). The anomalous winds advect the background high moisture in such a way that they increases the lower-tropospheric moisture over the initiation region (20°S-0°N, 50°E-70°E).

The advection of the perturbation moisture by the mean flow, particularly from the northern boundary of the initiation domain, also contributes to the local moistening (Fig. 7b). A maximum anomalous specific humidity center is located on the north edge of the initiation domain. According to our calculation, this positive moisture anomaly is attributed to both the anomalous horizontal advection and the apparent moisture source (figure not shown). The background wind advects the anomalous moisture southward, leading to the increase of moisture in the initiation region.

The calculation of vertically integrated (from 1000 hPa to 700 hPa) intraseasonal heat budget shows that during the initiation period the positive temperature tendency is caused by both the horizontal advection and the descending-induced adiabatic warming (Fig. 8a). The diabatic heating, on the other hand, has a negative impact.

Similar to the moisture diagnosis, the air temperature and wind fields were decomposed into the LFBS, the intraseasonal and the high-frequency components (i.e., $T=\overline{T}+T'+T^*$, $u=\overline{u}+u'+u^*$, $v=\overline{v}+v'+v^*$). Figures 8b and 8c show that the largest contribution to the horizontal advection arises from the advection of the background temperature by the MJO flow and the largest contribution of the adiabatic warming arises from the anomalous descending motion. Other terms are generally small.

Figure 9 presents the horizontal patterns of lower-tropospheric mean temperature and anomalous wind fields averaged from day -25 to day -15. The maximum mean temperature appears along 10°S. The anomalous warm advection by the MJO flow leads to the increase of the lower-tropospheric temperature over the initiation region.

5. Circumnavigating upstream forcing versus downstream forcing

The moisture and heat budget analyses above reveals that the low-tropospheric moistening and warming prior to the MJO initiation are attributed to the anomalous wind forcing over the tropical Indian Ocean. A key issue then is what causes the generation of the anomalous wind. There are two possible sources in generating the anomalous wind. Firstly, the anomalous easterlies may be a direct Kelvin wave response to a positive MJO heating over western Pacific (see a schematic diagram in Fig 10a). This is possible as the preceding MJO convection travels eastward along the equator after initiated over the WIO. This represents an upstream forcing of the circumnavigating MJO mode. Secondly, the anomalous wind over the tropical Indian Ocean may be a direct Rossby wave response to a negative MJO heating over the EIO (see a schematic diagram in Fig. 10b). This is possible because a suppressed-phase MJO emerges in the WIO after a convective-phase MJO moves to the EIO; the suppressed-phase MJO then intensifies and moves eastward. This scenario represents a downstream forcing of an opposite-phase MJO in the EIO.

To illustrate what (upstream or downstream forcing effect) actually happens in real world, we plotted the composite OLR and 850-hPa wind evolution maps from day -25 to day 5 (Fig. 11). Note that the anomalous easterlies dominate over the equatorial Indian Ocean from day -25 to day -15. At day -25, a positive OLR center (representing the suppressed convective phase of

MJO) is located in the EIO, while a negative OLR center (representing the enhanced convective MJO phase) is located in the western equatorial Pacific. If the anomalous flow in the tropical Indian Ocean is a direct Kevin wave response to the positive heating in the western Pacific, one would expect continuous easterly anomalies across the Pacific and Atlantic basin and Africa. As one can see, the zonal wind anomaly is not continuous and is broken over the eastern equatorial Pacific at both day -25 and day -20 (see ellipsoids in Fig. 11). At day -15, the positive heating is so weak that westerly anomalies (rather than easterly anomalies) appear across the Pacific. During the initiation period there is an opposite trend between the anomalous wind over the Indian Ocean and the western Pacific heating anomaly. Whereas the local anomalous wind is strengthened from day -25 to day -15, the heating weakens as it moves slowly eastward. At day -15, the major branch of the MJO convection is confined to the west of the dateline. It is difficult to argue that such a weak heating is able to exert an upstream impact on the initiation of new MJO convection in the WIO. On the other hand, the strength and pattern of the anomalous wind over the Indian Ocean are closely related to the negative heating anomaly over the EIO. Therefore, Figure 11 presents observational evidence that the anomalous wind over the Indian Ocean is a direct Rossby wave response to the suppressed MJO heating over the EIO.

To further support the downstream forcing argument, we plotted the longitude-time section of the intraseasonal OLR and 850-hPa zonal wind anomalies averaged over 20°S-0°N (Fig. 12). While the zonal wind anomaly shows a conventional circumnavigation feature around the global tropics, the OLR anomaly exhibits a rather discontinuity characteristic, with a negative OLR anomaly in the WIO (around 60°E) occurring earlier than that over Africa. A similar discontinuity is found in the anomalous precipitation and lower-tropospheric specific humidity fields (figure not shown).

The evidence above suggests that the MJO initiation could not arise from the continuous eastward propagation of a preceding circumnavigating MJO mode; rather it arises from the setup of local potential instability induced by low-tropospheric circulation and moisture changes associated with the downstream forcing of a suppressed-phase MJO over the EIO.

The effect of the circumnavigating MJO mode can be further assessed through a set of idealized numerical experiments. To evaluate the role of the circumnavigating waves on the MJO, in the EXP_TA run, the eastward-propagating intraseasonal signal is greatly suppressed over the tropical Atlantic. Figure 13 shows the power spectrum of simulated intraseasonal OLR fields from both the control run and the EXP_TA run based on a wavenumber-frequency analysis. The magnitudes of averaged 20-90-day OLR spectrum for zonal wavenumber 1 in both the experiments are quite similar. This points out that the overall eastward-propagating MJO variance has little change even though the circumnavigating MJO mode is greatly suppressed.

To examine whether or not the suppression of the circumnavigating mode affects the convection initiation over the WIO, we plotted the variance map of 20-90-day filtered OLR fields for both the control and EXP_TA cases (Fig. 14). It is interesting to note that the averaged value of MJO variance in the initiation region is 660 W^2m^{-4} in the EXP_TA run, which is slightly larger than that (590 W^2m^{-4}) in the control run. Thus the numerical simulations support the notion that the circumnavigating mode has little contribution to the initiation of MJO convection over the WIO.

6. Mid-latitude wave activity flux and barotropic energy conversion

It has been shown from previous case studies (e.g., Hsu et al. 1990; Ray et al. 2009) that the mid-latitude perturbations may contribute to MJO initiation over the WIO. To examine this possible mid-latitude impact, we plotted the upper tropospheric (200 hPa) geopotential height anomaly pattern during the initiation period (Fig. 15). Note that the geopotential height anomaly displays a wave train pattern, with high pressure centers located southeast of South of America and southeast of Africa, and low-pressure centers in between and to the east of Madagascar.

To illustrate wave energy dispersion characteristics, we calculated a phase-independent wave activity flux following Takaya and Nakamura (2001),

$$W=\frac{1}{2|\bar{u}|}\begin{pmatrix}\bar{u}(\psi'^{2}_{x}-\psi'\psi'_{xx})+\bar{v}\left(\psi'_{x}\psi'_{y}-\psi'\psi'_{xy}\right)\\ \bar{u}\left(\psi'_{x}\psi'_{y}-\psi'\psi'_{xy}\right)+\bar{v}\left(\psi'^{2}_{y}-\psi'\psi'_{yy}\right)\end{pmatrix} \qquad (5)$$

where a bar and a prime denote the LFBS and the intraseasonal anomaly, W represents the horizontal wave activity flux, u and v are zonal and meridional wind velocity, and ψ denotes the streamfunction.

The so-calculated 200-hPa wave activity flux vector and the flux convergence during the initiation period (from day -25 to day -15) are plotted in Fig. 15. Over most of mid-latitude in the Southern Hemisphere, there are pronounced eastward wave activity fluxes, indicating that the Rossby wave energy propagates eastward. The eastward wave activity fluxes turn northward and converge onto the tropical Indian Ocean between 10°S-30°S. The wave flux convergence implies that the wave energy is accumulated over the region. A similar wave activity flux feature is also found in the lower-tropospheric geopotential height anomaly field (figure not shown), indicating that the Rossby wave train has an equivalent barotropic structure. Thus, SH mid-latitude Rossby

wave perturbations may trigger the MJO initiation in the tropical Indian Ocean through wave energy accumulation.

The role of the mid-latitude forcing effect is further examined through idealized numerical experiments. As described in section 2, the EXP_NS experiment was designed to eliminate the mid-latitude influence on the MJO. By comparing the intraseasonal OLR spectrum in the control and EXP_NS run (Fig. 16a and b), one can see that the intraseasonal variability in the tropics weakens significantly. For example, the averaged spectrum for zonal wavenumber 1 and 20-90-day period is reduced by 45%. Thus the numerical result confirms that the remote forcing from mid-latitudes is important in affecting the overall tropical MJO variance.

To understand the relative role of the SH and NH mid-latitude forcing effect, we conducted two additional experiments termed as "EXP_SH" and "EXP_NH" respectively. In EXP_SH (EXP_NH) run, we blocked the equatorward propagation of SH (NH) mid-latitude waves. Compared to the control run, the averaged spectrum for zonal wavenumber 1 and 20-90-day period in the EXP_SH (EXP_NH) is reduced by 42% (7%) (Fig. 16c and d). The sensitivity experiments result indicate that most of the spectrum reduction in EXP_NS is attributed to SH wave blocking. Therefore, the remote forcing from mid-latitude SH is crucial for triggering tropical convection associated with MJO.

In addition to the energy accumulation process, the intraseasonal perturbation in the WIO may obtain energy from the mean flow. This local energy transfer process is through barotropic energy conversion. According to Hoskins et al. (1983) and Simmons et al. (1983), the barotropic energy conversion may be calculated based on the following formula:

$$CK = \frac{v'^2 - u'^2}{2}\left(\frac{\partial \bar{u}}{\partial x} - \frac{\partial \bar{v}}{\partial y}\right) - u'v'\left(\frac{\partial \bar{u}}{\partial y} + \frac{\partial \bar{v}}{\partial x}\right) \qquad (6)$$

where a bar denotes the climatologic seasonal mean quantity, and a prime denotes the intraseasonal anomaly. A positive value of CK indicates an energy conversion from the mean flow to the perturbation, that is, the MJO gains kinetic energy from the mean flow.

Figure 17 shows the calculated barotropic energy conversion field averaged over the northern winter season. A positive CK is concentrated in the southern Indian Ocean (around 20°S-0°N). This indicates that the barotropic energy conversion due to the MJO-mean flow interaction always contributes positively to the initiation and growth of the intraseasonal perturbations over the Indian Ocean.

7. Conclusion and discussion

The precursor signals associated with MJO convection initiation over the western equatorial Indian Ocean in boreal winter are examined based on the diagnosis of observational and ERA-40 reanalysis data. A marked increase of the lower-tropospheric moisture and temperature occurs 5-10 days prior to the convection initiation. The increase of the low-tropospheric moisture and temperature enhances lower-tropospheric equivalent potential temperature and moist static energy, which help set up a convectively more unstable stratification and eventually lead to the onset of the MJO convection over the WIO.

The diagnosis of the lower-tropospheric moisture budget shows that the moisture increase prior to the MJO initiation is caused primarily by anomalous horizontal advection. The vertical advection (associated with anomalous descending motion and lower-tropospheric divergence) plays a negative role. A further separation of the mean and perturbation motion shows that the horizontal moisture advection is mainly attributed to the advection of the mean specific humidity

by the MJO flow. The diagnosis of the lower-tropospheric heat budget shows that the temperature increase prior to the MJO initiation is primarily caused by the adiabatic warming associated with anomalous descending motion and the anomalous horizontal advection of the mean temperature by the MJO flow.

The moisture and heat budget analyses above indicate that the moisture and temperature precursor signals are primary induced by anomalous winds. Whether or not the anomalous local circulation is due to the upstream forcing of the circumnavigating MJO mode or a downstream forcing over the EIO is investigated through the analysis of both the observational data and idealized numerical experiment output. While the equatorial zonal wind anomaly shows more smooth eastward phase propagation around the globe, the OLR, precipitation and lower-tropospheric specific humidity anomalies exhibit a rather discontinuity characteristic, with the convection initiation over the WIO occurring earlier than that over Africa. Prior to the initiation, the major branch of the preceding MJO convection is confined to the west of the dateline. In response to the heating, anomalous easterlies appear to the east of the heating center. However, the easterly anomaly does not extend all the way to the WIO. It is discontinuous over the eastern equatorial Pacific (Fig. 11). Thus it is unlikely that the wind anomaly over the Indian Ocean is affected by the positive heating anomaly over the western Pacific. It is found that the local wind anomaly is more closely linked to the forcing of a negative heating anomaly over the EIO, suggesting a downstream Rossby wave forcing scenario. An idealized numerical experiment with the circumnavigating MJO mode being suppressed supports this claim. Compared to the control experiment, the MJO variance in the idealized experiment does not change much. The observational and modeling results imply that the local precursor signals are

mainly set up by the preceding suppressed-phase MJO over the EIO in the form of a Rossby wave response.

Our analysis suggests that the energy propagation and accumulation of SH mid-latitude Rossby waves is another possible triggering mechanism for MJO initiation over the WIO. A calculation of the Rossby wave activity flux shows that there is wave energy accumulation over the MJO initiation region. The possible SH mid-latitude impact on the tropical intraseasonal variability is further supported by an idealized numerical experiment that prohibits the energy and phase propagation of SH mid-latitude perturbations toward the tropics. The NH mid-latitude impact supported by sensitivity experiments is modulating the MJO period.

It is found that positive barotropic energy conversion appears in the MJO initiation region. This implies that the seasonal mean flow may provide kinetic energy to MJO disturbance and thus may be responsible for the initiation and development of intraseasonal perturbations over the tropical Indian Ocean.

The result presented from this study is different from Kikuchi and Takayabu (2003, KT hereafter), who emphasized the role of circumnavigating signal in MJO initiation. Note that KT constructed the MJO signal using extended EOF patterns in a global tropics domain. While this methodology can capture dominant large-scale propagation features, it greatly underestimates (or smoothes out) regional scale features associated with MJO convection initiation in WIO. For instance, according to KT's Fig. 5, the convection initiation appears at 60°E around t=4. Before this initiation time, low-level wind is a pronounced westerly anomaly, which is opposite to our result (we noted significant easterly anomaly signals prior to the initiation). Secondly, total precipitable water (TPW) used in KT is a vertically-integrated variable, which is approximately in phase with the precipitation anomaly (see KT's Fig. 5); thus the TPW does not lead the

convection. However, in the current analysis we noted that a key precursor signal is lower-tropospheric specific humidity, which leads the convection anomaly by 5-10 days.

One issue related to the MJO initiation is whether the local forcing in the tropics and the remote forcing from mid-latitudes are independent. In the current work we examined the composite evolution patterns based on the 20-yr analysis period (total 55 cases). Our composite patterns show that both the internal tropical process and the external mid-latitude forcing processes happened during the initiation period (day -25 to day -15). However, for each individual case, the two processes may occur on the same time and independently. From a physical mechanism point of view, the two processes are very different. One emphasizes low-level moisture advection process, and the other emphasizes upper-tropospheric Rossby wave energy propagation and accumulation. The former may trigger the convection through the gradual setup of a convectively unstable stratification, whereas the latter may trigger MJO perturbation through upper-tropospheric potential vorticity (PV) invasion. A related issue is the cause of irregularity of MJO. The timing between MJO events is highly variable, whereas the postulated downstream Rossby wave response would seem to have a more tightly bound periodicity. Thus it is reasonable to hypothesize that the horizontal advection of mean specific humidity by MJO flow keep moistening lower troposphere in the WIO until a trigger (from extratropics perhaps) comes along. In this case, low-level moistening is a necessary but not a sufficient condition for MJO initiation. On the other hand, not all individual MJO events may experience a gradual moistening before initiation. Thus a further study is needed to identify the relative roles of the tropical and extratropical triggering processes. In the subsequent study we will examine each of individual MJO events (from both the observational and model data) to reveal the relationship between the tropical and extratropical forcing.

Another issue is how the current analysis result depends on data. In this study we used the ERA-40 reanalysis data. A preliminary sensitivity test using different datasets such as NCEP Climate Forecast System Reanalysis (CFSR) and NASA Modern Era Retrospective-Analysis for Research and Applications (MERRA) shows that precursor signals obtained in the present study are robust across different datasets. This adds confidence to the present observational analysis.

Acknowledgement. The authors would like to thank Dr. Xinyao Rong for running ECHAM4 experiments. This work was supported by National Basic Research Program of China (2010CB951904), NSFC grant 41125017, NSF grant AGS-1106536, NOAA grant NA11OAR4310087, and by the International Pacific Research Center that is sponsored by the Japan Agency for Marine-Earth Science and Technology (JAMSTEC), NASA (NNX07AG53G) and NOAA (NA17RJ1230). This is SOEST contribution number xxxx and IPRC contribution number xxx.

Reference

Bladé, I., and D. L. Hartmann, 1993: Tropical intraseasonal oscillation in a simple nonlinear model. *J. Atmos. Sci.*, **50**, 2922-2939.

Fu, X., B. Wang, and T. Li, 2002: Impacts of air-sea coupling on the simulation of the mean Asian summer monsoon in the ECHAM-4 model. *Mon. Wea. Rev.*, **130** (12), 2889-2904.

Fu, X., B. Wang, Q. Bao, P. Liu, and J. Lee, 2009: Impacts of initial conditions on monsoon intraseasonal forecasting. *Geophys. Res. Lett.*, **36**, L08801, doi: 10.1029/2009GL 037166.

Gill, A. E., 1980: Some simple solutions for heat-induced tropical circulation. *Quart. J. Roy. Meteor. Soc.*, **106**, 447-462.

Hoskins, B. J., I. N. James, and G. H. White, 1983: The shape, propagation and mean-flow interaction of large-scale weather system. J. Atmos. Sci., **40**, 1595-1612.

Hsu, H.-H., and M. Lee, 2005: Topographic effects on the eastward propagation and initiation of the Madden–Julian oscillation. J. Climate, **18**, 795-809.

Hsu, H.-H., B. J. Hoskins, and F.-F. Jin, 1990: The 1985/86 intraseasonal oscillation and the role of the extratropics. J. Atmos. Sci., **47**, 823-839.

Hsu, P.-C., and T. Li, 2012: Role of the boundary layer moisture asymmetry in causing the eastward propagation of the Madden-Julian Oscillation. J. Climate, in press.

Hu, Q., and D. A. Randall, 1994: Low-frequency oscillation in radiative–convective systems. J. Atmos. Sci., **51**, 1089-1099.

Jiang, X., T. Li, and B. Wang, 2004: Structures and mechanisms of the northward propagating boreal summer intraseasonal oscillation. J. Climate, **17**, 1022-1039.

Jiang, X. and T. Li, 2005: Reinitiation of the boreal summer intraseasonal oscillation in the tropical Indian Ocean. J. Climate, **18**, 3777-3795.

Kemball-Cook, S. R., and B. C. Weare, 2001: The onset of convection in the Madden-Julian oscillation. J. Climate, **14**, 780-793.

Kemball-Cook, S., and B. Wang, 2001: Equatorial waves and air-sea interaction in the boreal summer intraseasonal oscillation. J. Climate, **14**, 2923-2942.

Kessler, W. S., 2001: EOF representations of the Madden-Julian oscillation and its connection with ENSO. J. Climate, **14**, 3055-3061.

Kikuchi, K., and Y. N. Takayabu, 2003: Equatorial circumnavigation of moisture signal associated with the Madden-Julian Oscillation (MJO) during boreal winter. J. Meteor. Soc. Japan, **81**, 851-869.

Kiladis, G. N., and K. M. Weickmann, 1992: Circulation anomalies associated with tropical convection during northern winter. Mon. Wea. Rev., **120**, 1900-1923.

Lau, K.-M., and L. Peng, 1987: Origin of low-frequency (intraseasonal) oscillations in the tropical atmosphere. Part I: Basic theory. J. Atmos. Sci., **44**, 950-972.

Li, T., and C. Zhou, 2009: Planetary Scale Selection of the Madden-Julian Oscillation. J. Atmos. Sci, **66**, 2429-2443.

Li, T., F. Tam, X. Fu, T.-J. Zhou, W.-J. Zhu, 2008: Causes of the Intraseasonal SST Variability in the Tropical Indian Ocean, Atmos. and Oceanic Sci. Lett., **1**, 18-23.

Liebmann, B., and C. A. Smith, 1996: Description of a complete (interpolated) outgoing longwave radiation dataset. Bull. Amer. Meteor. Soc., **77**, 1275-1277.

Lin, H., G. Brunet, and J. Derome, 2007: Intraseasonal Variability in a Dry Atmospheric Model. J. Atmos. Sci., **64**, 2422-2441.

Lin, J.-L., G. N. Kiladis, B. E. Mapes, K. M. Weickmann, K. R. Sperber, W. Lin, M. C. Wheeler, S. D. Schubert, A. Del Genio, L. .J. Donner, S. Emori, J.-F. Gueremy, F. Hourdin, P. J. Rasch, E. Roeckner, and J. F. Scinocca, 2006: Tropical intraseasonal variability in 14 IPCC AR4 climate models. Part I: Convective signals. J. Climate, **19**, 2665-2690.

Lin, J. W. B., J. D. Neelin, and N. Zeng, 2000: Maintenance of tropical intraseasonal variability: Impact of evaporation-wind feedback and mid-latitude storms, J. Atmos. Sci., **57**, 2793-2823.

Madden, R. A., and P. R. Julian, 1971: Detection of a 40-50 day oscillation in the zonal wind in the tropical Pacific. J. Atmos.Sci., **28**, 702-708.

Madden, R. A., and P. R. Julian, 1972: Description of global-scale circulation cells in the tropics with a 40-50 day period. J. Atmos. Sci., **29**, 1109-1123.

Maloney, E., and D. L. Hartmann, 1998: Frictional moisture convergence in a composite life cycle of the Madden-Julian oscillation. J. Climate, **11**, 2387–2403.

Maloney, E., A. H. Sobel, and W. M. Hannah, 2010: Intraseasonal variability in an aquaplanet general circulation model. J. Adv. Model. Earth Syst., 2, Art. #5, 24 pp., doi:10.3894/ JAMES. 2010.2.5.

Matthews, A. J., 2000: Propagation mechanisms for the Madden-Julian oscillation. Quart. J. Roy. Meteor. Soc., **126**, 2637-2651.

Matthews, A. J., 2008: Primary and successive events in the Madden-Julian Oscillation. Quart. J. Roy. Meteor. Soc., **134**, 439- 453.

Matthews, A. J., and G. N. Kiladis, 1999: The tropical-extratropical interaction between high-frequency transients and the Madden–Julian oscillation. Mon. Wea. Rev., **127**, 661-677.

Pan, L. and T. Li, 2007: Interactions between the tropical ISO and mid-latitude low-frequency flow. Clim. Dyn., DOI: 10.1007/s00382-007-0272-7.

Ray, P., C. Zhang, J. Dudhia, S. S. Chen, 2009: A Numerical Case Study on the Initiation of the Madden-Julian Oscillation. J. Atmos. Sci., **66**, 310-331.

Raymond, D. J., 2000: Thermodynamic control of tropical rainfall. Quart. J. Roy. Meteor. Soc., **126**, 889-898.

Roeckner, E., and Coauthors, 1996: The atmospheric general circulation model ECHAM-4: Model description and simulation of present-day climate. Max-Planck-Institut for Meteorologie Rep. 218, Hamburg, Germany , 90 pp.

Seo, K.-H., and K.-Y. Kim, 2003: Propagation and initiation mechanisms of the Madden-Julian oscillation. J. Geophys. Res., 108, 4384, doi: 10.1029/2002JD002876.

Simmons, A. J., J. M. Wallace, and W. Branstator, 1983: Barotropic wave propagation and instability, and atmospheric teleconnection patterns. J. Atmos. Sci., **40**, 1363-1392.

Sobel, A. H., and H. Gildor, 2003: A simple time-dependent model of SST hot spots. J. Climate, **16**, 3978-3992.

Slingo, J. M., D. P. Rowell, K. R. Sperber, and F. Norley, 1999: On the predictability of the interannual behaviour of the Madden-Julian Oscillation and its relationship with El Niño. Quart. J. Roy. Meteor. Soc., **125**, 583-609.

Takaya, K. and H. Nakamura, 2001: A formulation of a phase-independent wave-activity flux for stationary and migratory quasigeostrophic eddies on a zonally varying basic flow. J. Atmos. Sci., **58**, 608-627.

Teng, H., and B. Wang, 2003: Interannual variations of the boreal summer intraseasonal oscillation in the Asian–Pacific region. J. Climate, **16**, 3572-3584.

Uppala, S. M. and 45 Coauthors, 2005: The ERA-40 Reanalysis. Quart. J. Roy. Meteorol. Soc., **131**, 2961-3012.

Wang, B., and T. Li, 1994: Convective interaction with boundary layer dynamics in the development of a tropical intraseasonal system. J. Atmos. Sci., **51**, 1386-1400.

Wheeler, M., and H. H. Hendon, 2004: Anall-season real-time multivariate MJO index: Development of an index for monitoring and prediction. Mon. Wea. Rev., **132**, 1917-1932.

Yanai, M. S., S., Esbensen, and J. H. Chu, 1973: Determination of bulk properties of tropical cloud clusters from large-scale heat and moisture budgets. J. Atmos. Sci., **30**, 611-627.

Zhang, G.-J. and X. Song, 2009: Interaction of deep and shallow convection is key to Madden-Julian Oscillation simulation. Geophys. Res. Lett., **36**, doi:10.1029/2009GL03740.

Table Captions

Table 1. List of Numerical Experiments

Figure Captions

Fig. 1 Patterns of (a) first and (b) second EOF modes of intraseasonal OLR during November-April. (c) Lagged correlation coefficients between the time series of the two leading EOF modes; positive coefficients in (c) mean that the second EOF mode leads the first one. (d) Time series of the first EOF mode during the 20-year (1982-2001) period; a red line represents the value of one standard deviation.

Fig. 2 Horizontal distribution of 20-90-day filtered OLR variance (unit: W^2m^{-4}) during November-April, 1982-2001.

Fig. 3 Evolution of the composite OLR (unit: Wm^{-2}) pattern from day -9 to day 0 at a 3-day interval. The negative OLR represents enhanced MJO convection. Day 0 corresponds to the peak of time series of the first EOF mode for each of selected strong MJO cases.

Fig. 4 Evolutions of (a) the composite intraseasonal OLR anomaly and (b-f) vertical profiles of intraseasonal vertical velocity, specific humidity, temperature, equivalent potential temperature (θ_e) and moist static energy (MSE) fields averaged over the MJO initiation region (50°-70°E, 20°S-0°N).

Fig. 5 (Top) Evolutions of the potential instability parameter $\Delta\theta_e$ (green curve), lower-tropospheric θ_e (θ_{eL}, averaged over 700-1000hPa, blue curve), and middle-tropospheric θ_e ($\theta_{eM,}$ averaged over 300-400hPa, red curve). (Bottom) Change of the θ_{eL} (unit: K) from day -25 to day -15 (red bar) and contributions to the θ_{eL} change due to lower-tropospheric temperature (green

bar) and specific humidity (blue bar) variations.

Fig. 6 (a) 1000hPa-700 hPa integrated intraseasonal moisture budget terms averaged during the period of day -25 to day -15 over 50°-70°E, 20°S-0°N. From left to right: observed specific humidity tendency, horizontal moisture advection, vertical moisture advection, apparent moisture source, and sum of the last three terms. (b) Individual components of the horizontal moisture advection term. (c) Vertical profiles of the apparent moisture source term.

Fig. 7 Vertically integrated (1000hPa-700hPa) intraseasonal wind and LFBS specific humidity fields (top) and vertically integrated intraseasonal specific humidity and LBFS wind fields (bottom) averaged during the initiation period (day -25 to day -15).

Fig. 8 (a) Vertically-integrated (1000hPa-700hPa) intraseasonal temperature budget terms during the initiation period (from day -25 to day -15) over 50°-70°E, 20°S-0°N. (b) Individual components of the horizontal temperature advection. (c) Individual components of the adiabatic term (from left to right): $(\bar{\omega}\frac{R\bar{T}}{c_p p}-\bar{\omega}\frac{\partial\bar{T}}{\partial p})'$, $(\bar{\omega}\frac{RT'}{c_p p}-\bar{\omega}\frac{\partial T'}{\partial p})'$, $(\bar{\omega}\frac{RT^*}{c_p p}-\bar{\omega}\frac{\partial T^*}{\partial p})'$, $(\omega'\frac{R\bar{T}}{c_p p}-\omega'\frac{\partial\bar{T}}{\partial p})'$, $(\omega'\frac{RT'}{c_p p}-\omega'\frac{\partial T'}{\partial p})'$, $(\omega'\frac{RT^*}{c_p p}-\omega'\frac{\partial T^*}{\partial p})'$, $(\omega^*\frac{R\bar{T}}{c_p p}-\omega^*\frac{\partial\bar{T}}{\partial p})'$, $(\omega^*\frac{RT'}{c_p p}-\omega^*\frac{\partial T'}{\partial p})'$, $(\omega^*\frac{RT^*}{c_p p}-\omega^*\frac{\partial T^*}{\partial p})'$.

Fig. 9 Vertically integrated (1000hPa-700hPa) intraseasonal wind and LFBS temperature fields averaged during the initiation period (day -25 to day -15).

Fig. 10 Schematic diagrams illustrating a) an upstream forcing scenario in which a positive MJO heating in the western Pacific may induce an anomalous easterly over the WIO through Kelvin wave response and b) a downstream forcing scenario in which a negative heating anomaly associated with suppressed-phase MJO may induce twin-gyre circulation in the tropical Indian

Ocean through Rossby wave response.

Fig. 11 Evolution of the composite OLR (color; unit: Wm^{-2}) and 850-hPa wind (vector; unit: ms^{-1}) patterns from day -25 to day 5 at an interval of 5 days.

Fig. 12 Time-longitude section of the composite OLR (color; unit: Wm^{-2}) and 850hPa zonal wind (contour; unit: ms^{-1}) anomalies averaged along 20°S-0°N.

Fig. 13 The wavenumber-frequency spectra (unit: W^2m^{-4}) of the intraseasonal OLR anomaly derived from the 20-yr simulation of the Control and EXP_TA experiments. The spectrum analysis was done for a limited domain over (40°E-180°E, 20°N-20°S).

Fig. 14 Horizontal distribution of 20-90-day filtered OLR variance (unit: W^2m^{-4}) in boreal winter derived from the Control and EXP_TA experiments.

Fig. 15 20-90-day filtered observed geopotential height anomaly (contour, unit: m^2s^{-2}), Rossby wave activity flux (vector, unit: m^2s^{-2}) and wave flux divergence (color, unit: 10^{-5} ms^{-2}, only negative values are shaded over the Indian Ocean) at 200 hPa during the initiation period from day -25 to day -15.

Fig. 16 Same as Fig. 13 except for the Control, EXP_NS, EXP_SH and EXP_NH experiments.

Fig. 17 Horizontal distribution of the 850-hPa barotropic energy conversion field (color, unit: 10^{-5} m^2s^{-3}) and the seasonal mean 850-hPa wind field (vector, unit: ms^{-1}).

Table 1. List of Numerical Experiments

Experiment	Description	Purpose
Control	ECHAM4 atmosphere only, forced by the climatological monthly SST	MJO evaluation; Provide controlled annual cycle conditions for other experiments
EXP_TA	Relaxed to the annual cycle derived from the control run over the tropical Atlantic	To evaluate the role of the circumnavigating MJO mode
EXP_NS	Relaxed to the annual cycle derived from the control run over 20°S-30°S and 20°N-30°N	To evaluate the role of the mid-latitude influence
EXP_SH	Relaxed to the annual cycle derived from the control run over 20°S-30°S	To evaluate the role of the SH mid-latitude influence
EXP_NH	Relaxed to the annual cycle derived from the control run over 20°N-30°N	To evaluate the role of the NH mid-latitude influence

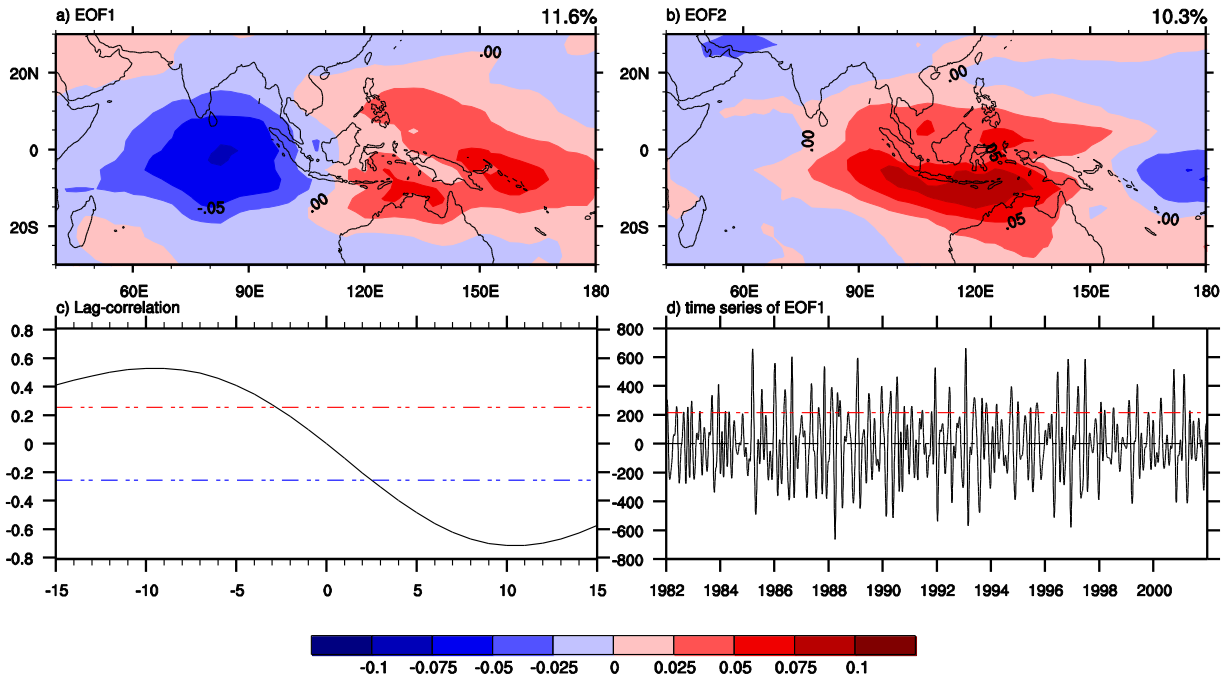

Fig. 1 Patterns of (a) first and (b) second EOF modes of intraseasonal OLR during November-April. (c) Lagged correlation coefficients between the time series of the two leading EOF modes; positive coefficients in (c) mean that the second EOF mode leads the first one. (d) Time series of the first EOF mode during the 20-year (1982-2001) period; a red line represents the value of one standard deviation.

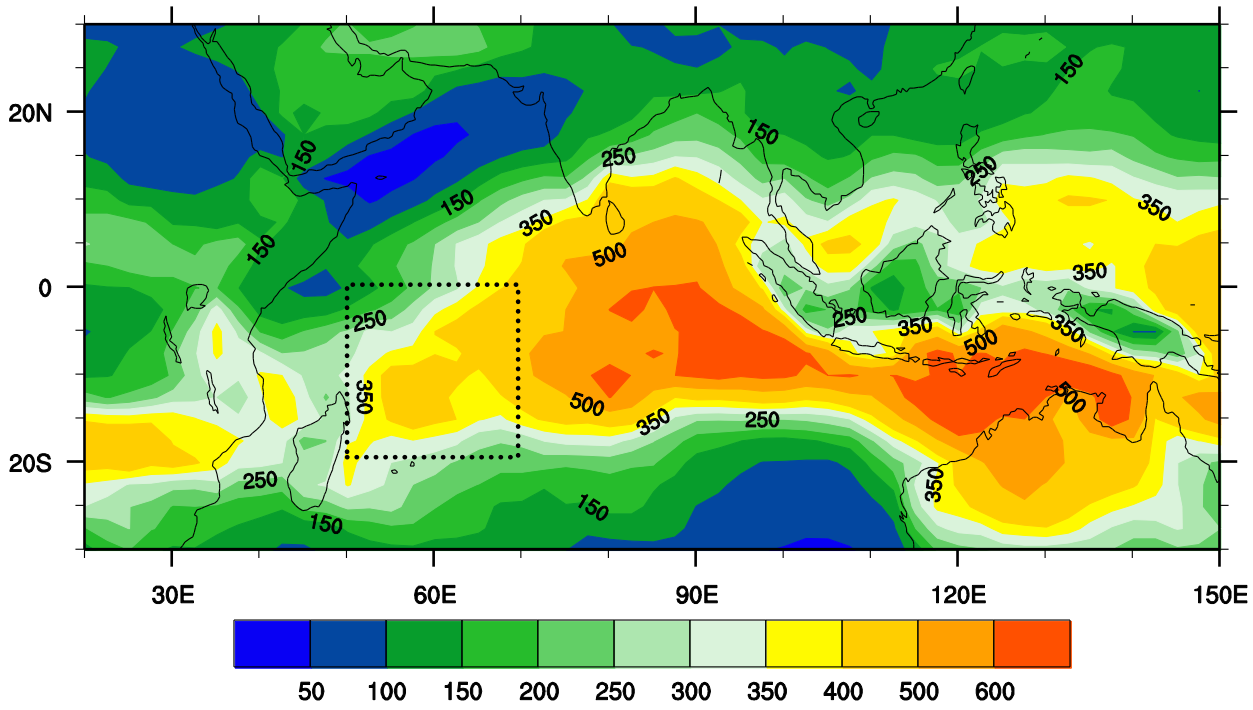

Fig. 2 Horizontal distribution of 20-90-day filtered OLR variance (unit: W^2 m^{-4}) during November-April, 1982-2001.

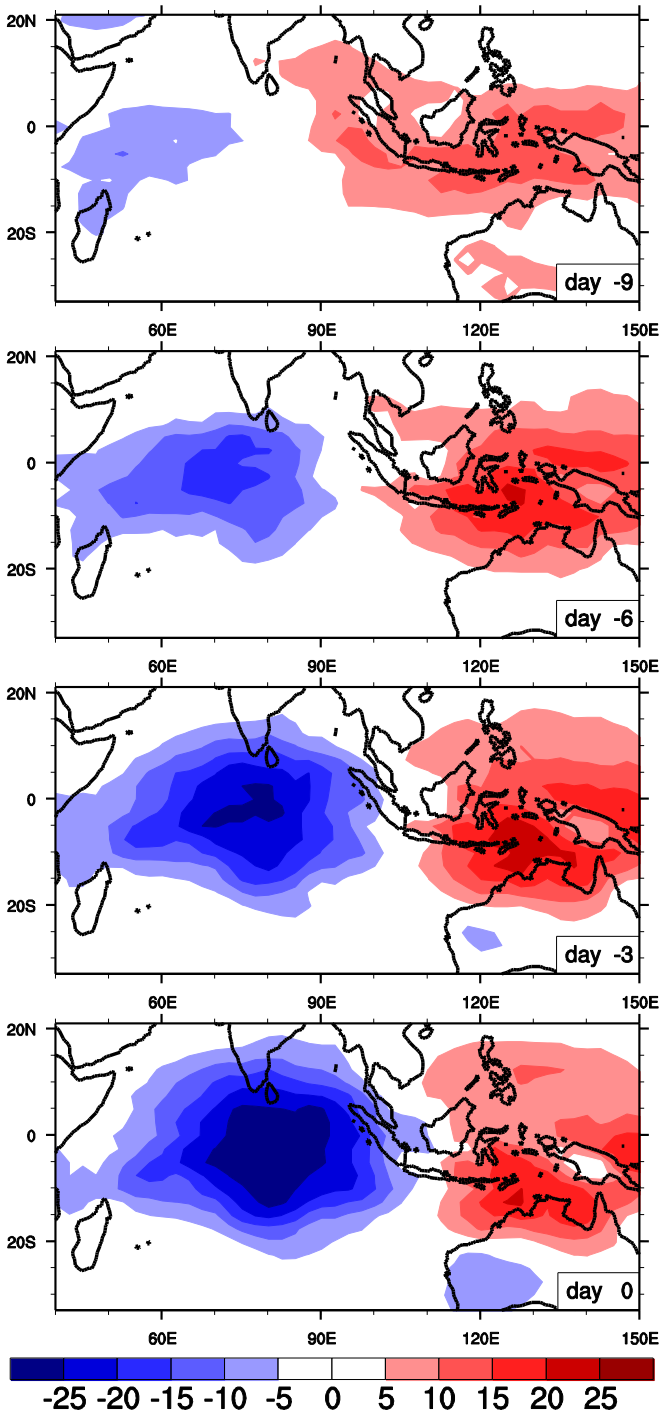

Fig. 3 Evolution of the composite OLR (unit: W m-2) pattern from day -9 to day 0 at a 3-day interval. The negative OLR represents enhanced MJO convection. Day 0 corresponds to the peak of time series of the first EOF mode for each of selected strong MJO cases.

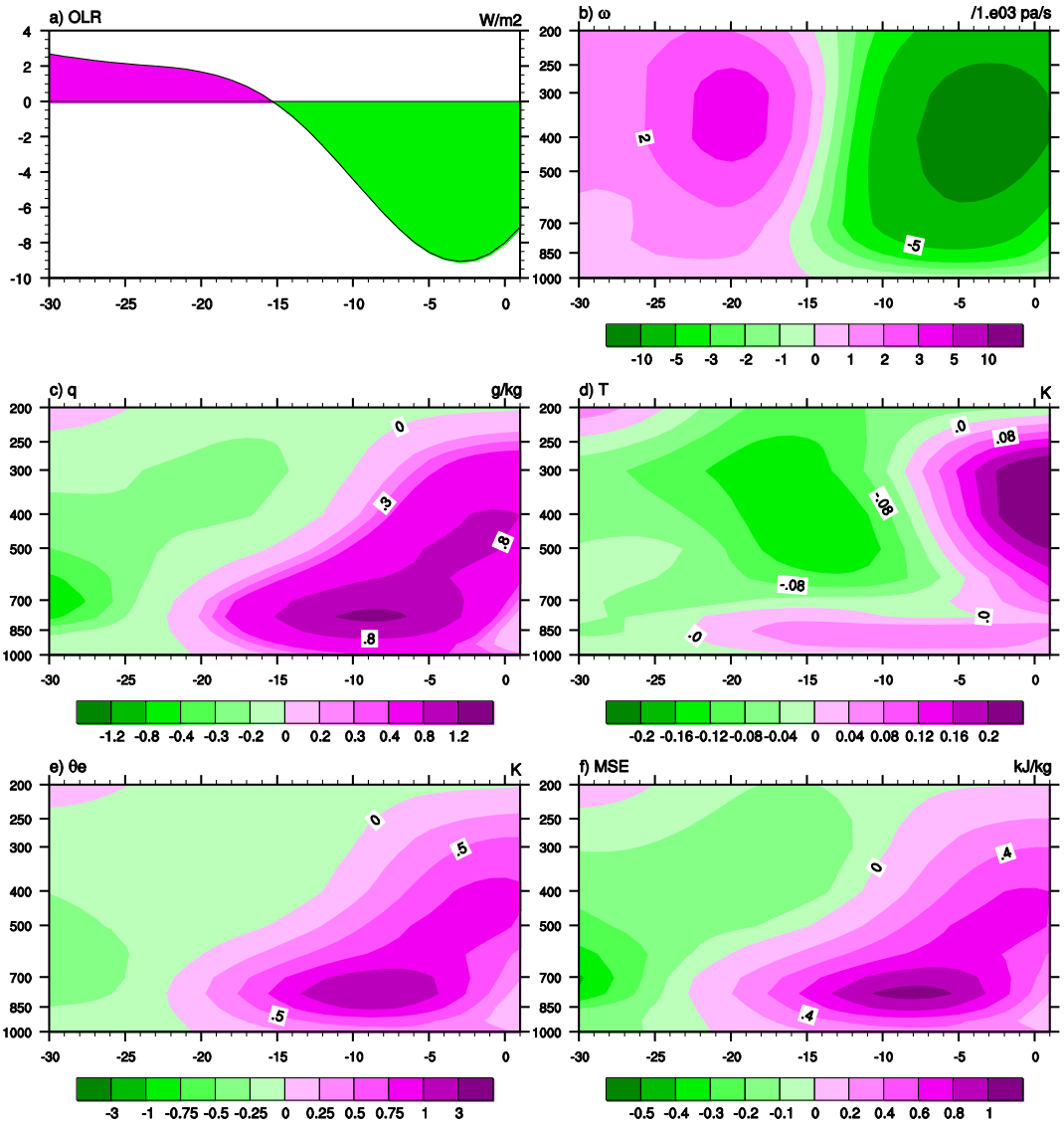

Fig. 4 Evolutions of (a) the composite intraseasonal OLR anomaly and (b-f) vertical profiles of intraseasonal vertical velocity, specific humidity, temperature, equivalent potential temperature (θ_e) and moist static energy (MSE) fields averaged over the MJO initiation region (50°-70°E, 20°S-0°N).

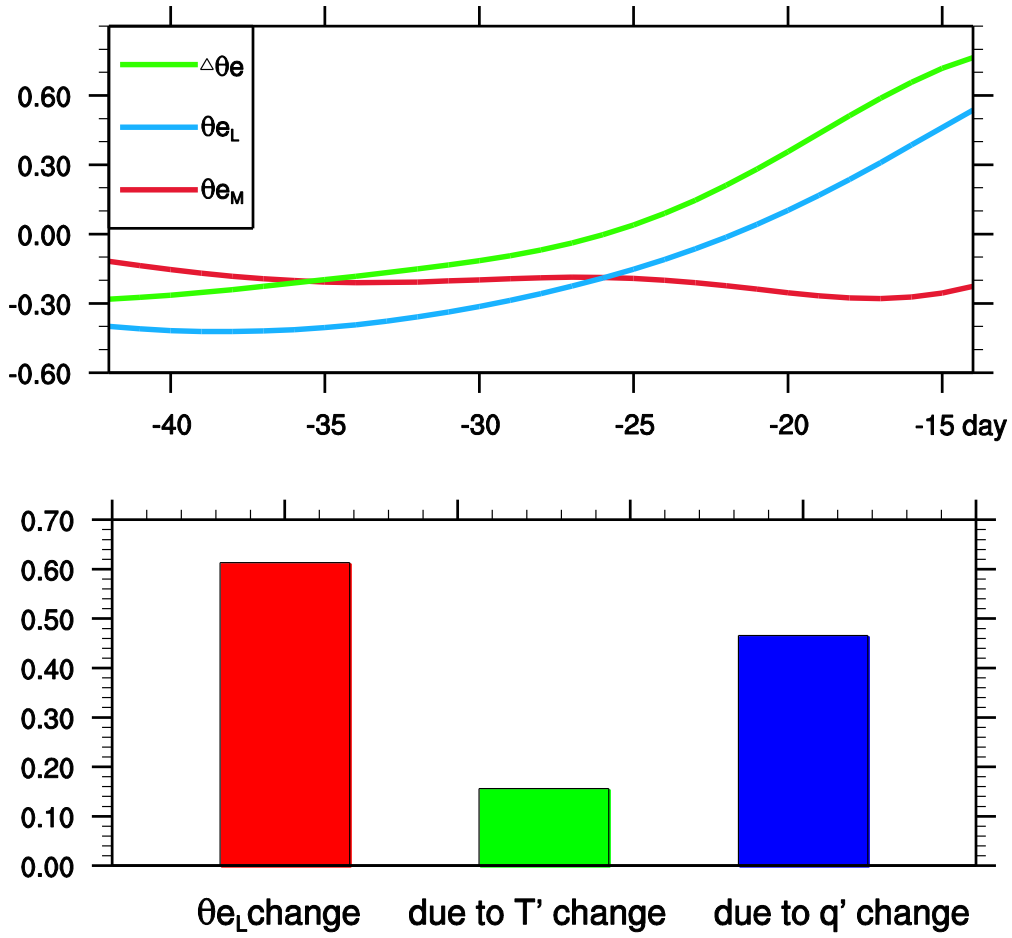

Fig. 5 (Top) Evolutions of the potential instability parameter $\Delta\theta_e$ (green curve), lower-tropospheric θ_e (θ_{eL}, averaged over 700-1000hPa, blue curve), and middle-tropospheric θ_e (θ_{eM}, averaged over 300-400hPa, red curve). (Bottom) Change of the θ_{eL} (unit: K) from day -25 to day -15 (red bar) and contributions to the θ_{eL} change due to lower-tropospheric temperature (green bar) and specific humidity (blue bar) variations.

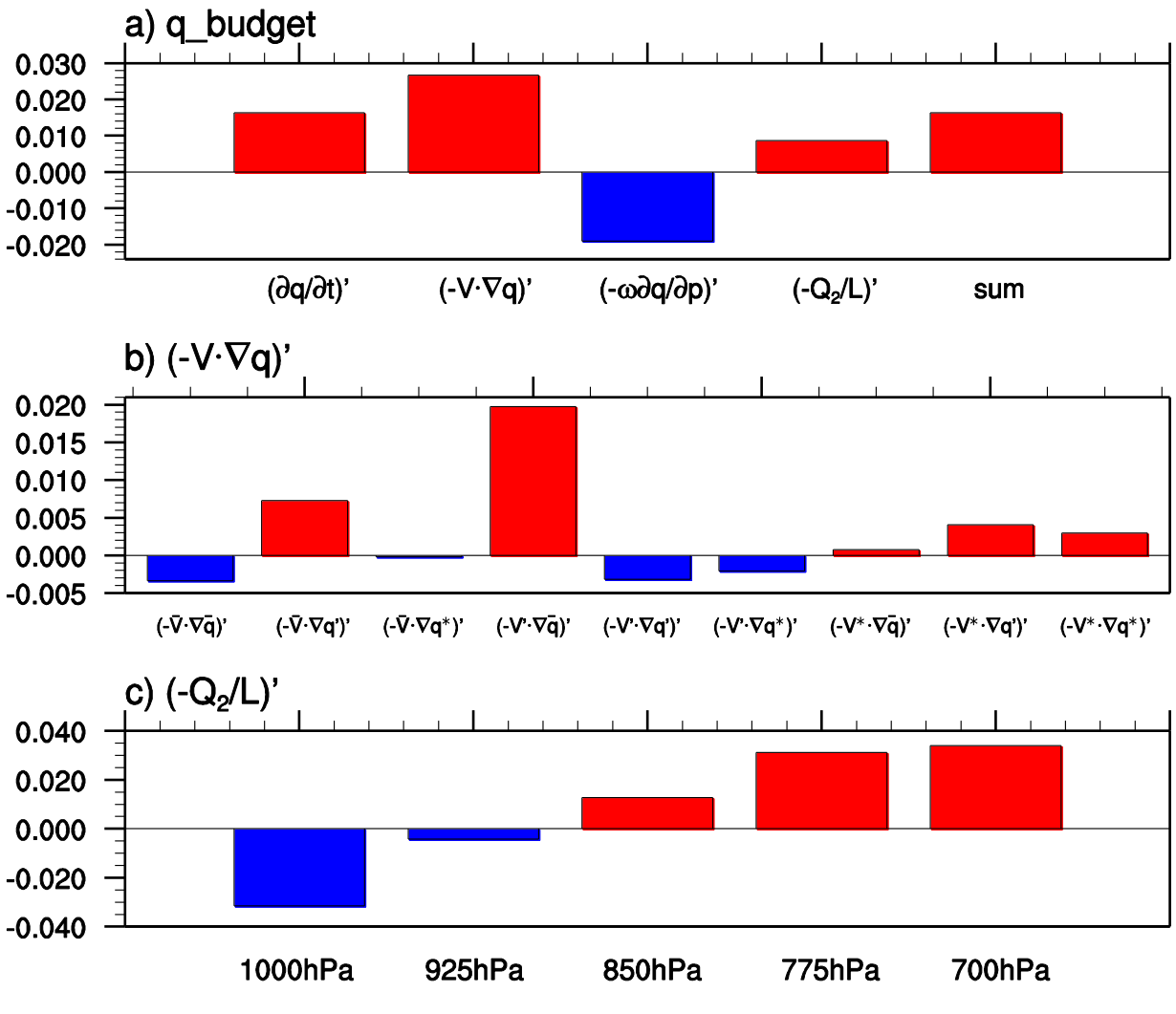

Fig. 6 (a) 1000hPa-700hPa integrated intraseasonal moisture budget terms averaged during the period of day -25 to day -15 over 50°-70°E, 20°S-0°N. From left to right: observed specific humidity tendency, horizontal moisture advection, vertical moisture advection, apparent moisture source, and sum of the last three terms. (b) Individual components of the horizontal moisture advection term. (c) Vertical profiles of the apparent moisture source term.

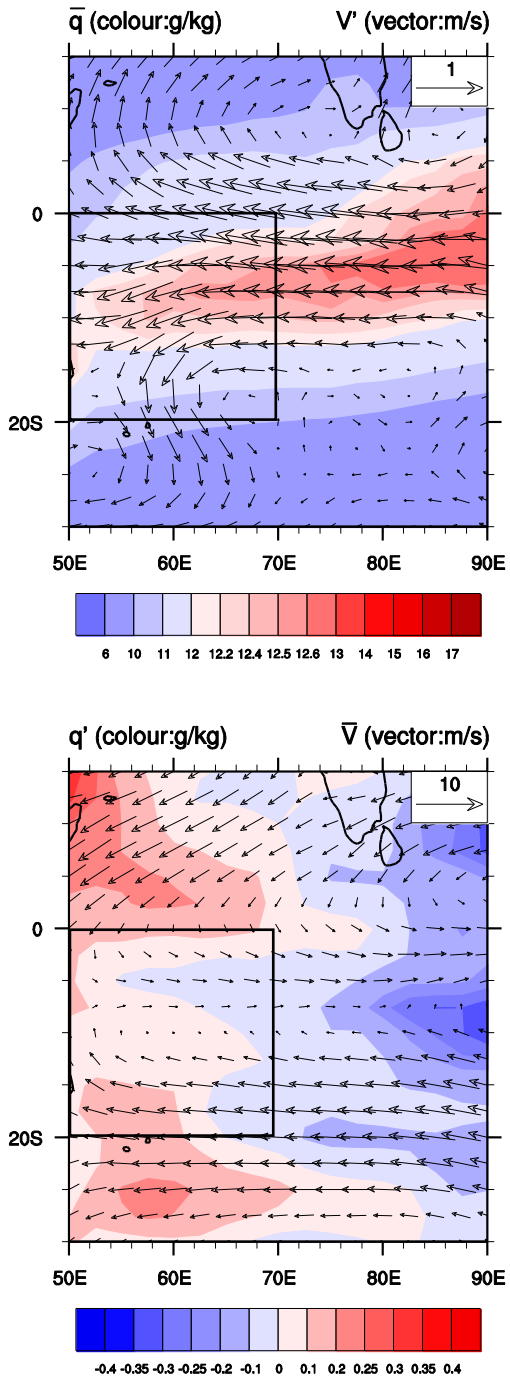

Fig. 7 Vertically integrated (1000hPa-700hPa) intraseasonal wind and LFBS specific humidity fields (top) and vertically integrated intraseasonal specific humidity and LBFS wind fields (bottom) averaged during the initiation period (day -25 to day -15).

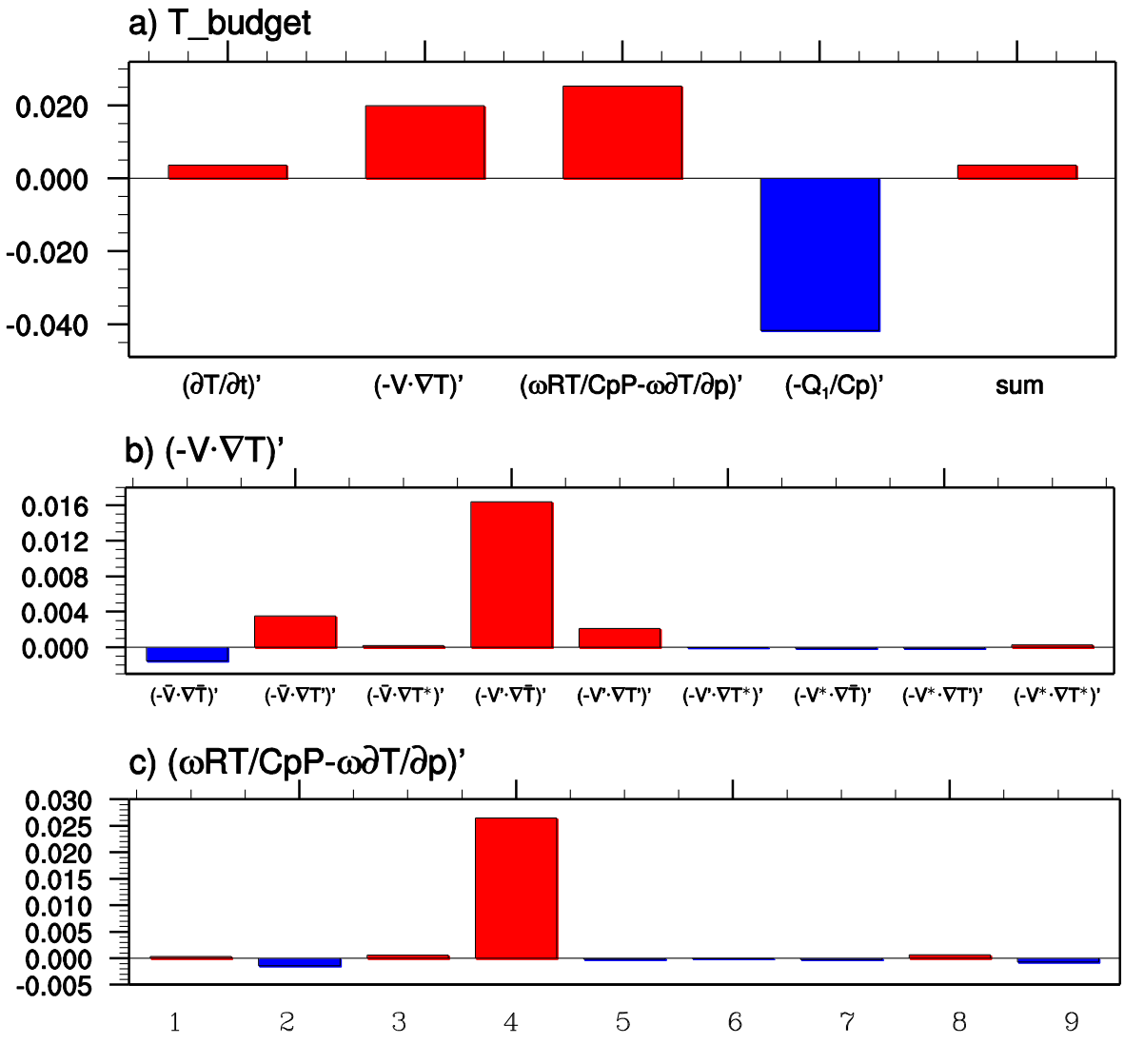

Fig. 8 (a) Vertically-integrated (1000hPa-700hPa) intraseasonal temperature budget terms during the initiation period (from day -25 to day -15) over 50°-70°E, 20°S-0°N. (b) Individual components of the horizontal temperature advection. (c) Individual components of the adiabatic term (from left to right): $(\bar{\omega}\frac{R\bar{T}}{c_p p}-\bar{\omega}\frac{\partial\bar{T}}{\partial p})'$, $(\bar{\omega}\frac{RT'}{c_p p}-\bar{\omega}\frac{\partial T'}{\partial p})'$, $(\bar{\omega}\frac{RT^*}{c_p p}-\bar{\omega}\frac{\partial T^*}{\partial p})'$, $(\omega'\frac{R\bar{T}}{c_p p}-\omega'\frac{\partial\bar{T}}{\partial p})'$, $(\omega'\frac{RT'}{c_p p}-\omega'\frac{\partial T'}{\partial p})'$, $(\omega'\frac{RT^*}{c_p p}-\omega'\frac{\partial T^*}{\partial p})'$, $(\omega^*\frac{R\bar{T}}{c_p p}-\omega^*\frac{\partial\bar{T}}{\partial p})'$, $(\omega^*\frac{RT'}{c_p p}-\omega^*\frac{\partial T'}{\partial p})'$, $(\omega^*\frac{RT^*}{c_p p}-\omega^*\frac{\partial T^*}{\partial p})'$.

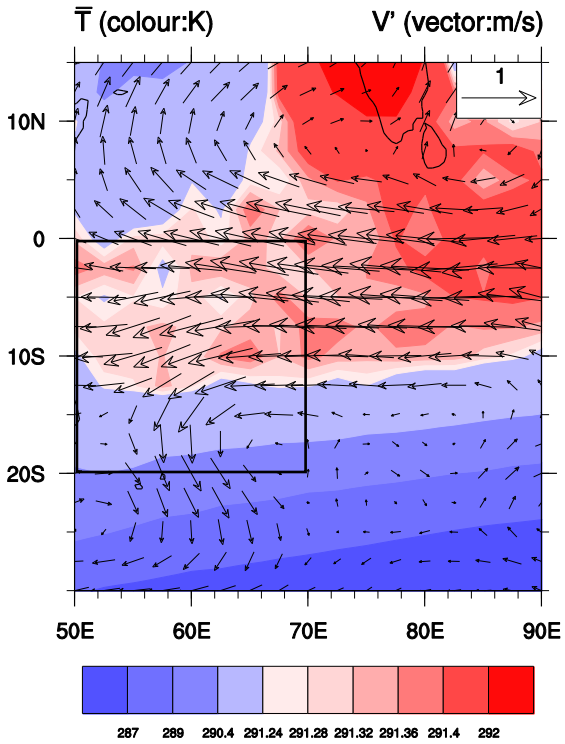

Fig. 9 Vertically integrated (1000hPa-700hPa) intraseasonal wind and LFBS temperature fields averaged during the initiation period (day -25 to day -15).

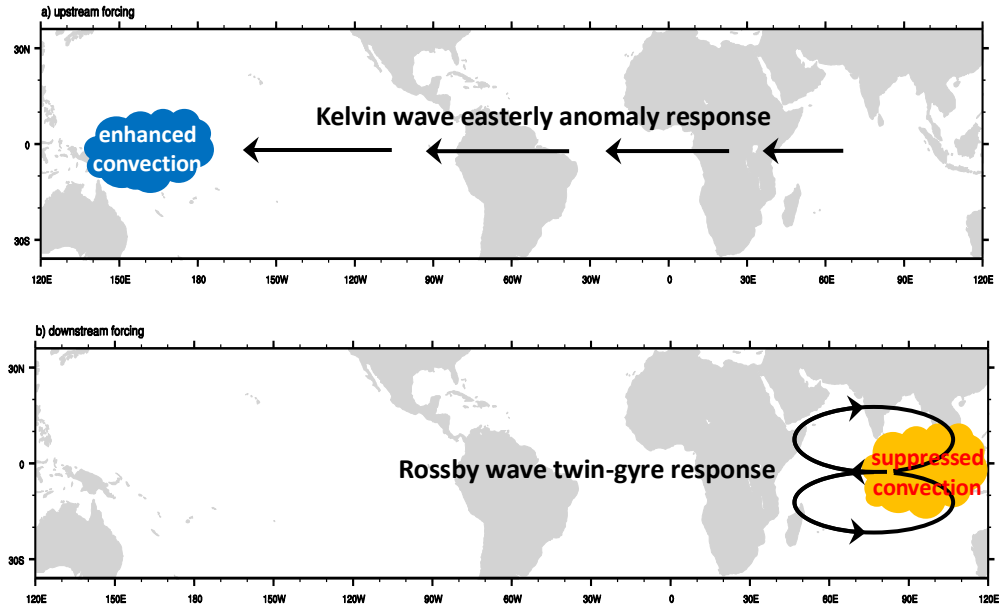

Fig. 10 Schematic diagrams illustrating a) an upstream forcing scenario in which a positive MJO heating in the western Pacific may induce an anomalous easterly over the WIO through Kelvin wave response and b) a downstream forcing scenario in which a negative heating anomaly associated with suppressed-phase MJO may induce twin-gyre circulation in the tropical Indian Ocean through Rossby wave response.

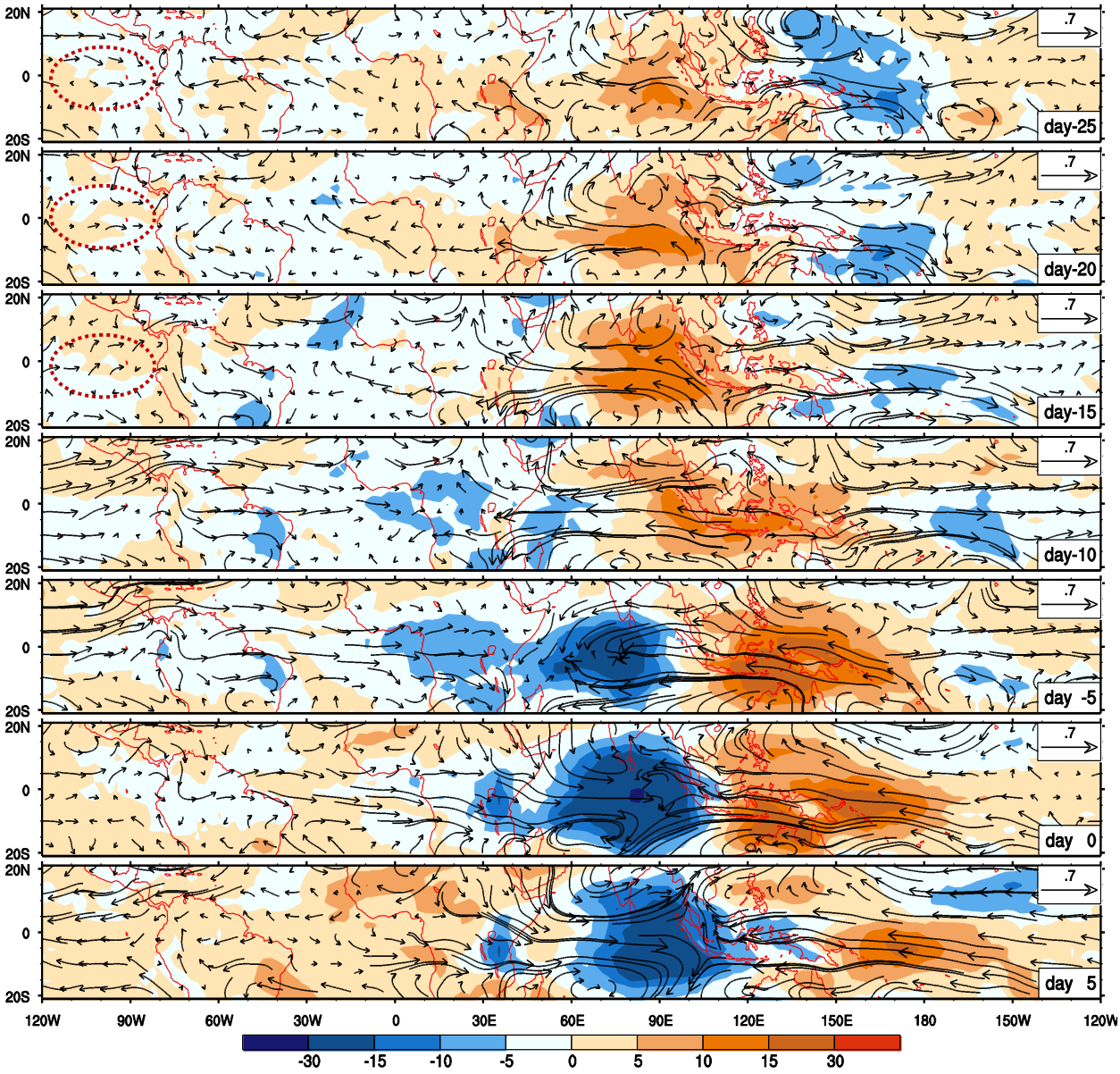

Fig. 11 Evolution of the composite OLR (color; unit: Wm^{-2}) and 850-hPa wind (vector; unit: ms^{-1}) patterns from day -25 to day 5 at an interval of 5 days.

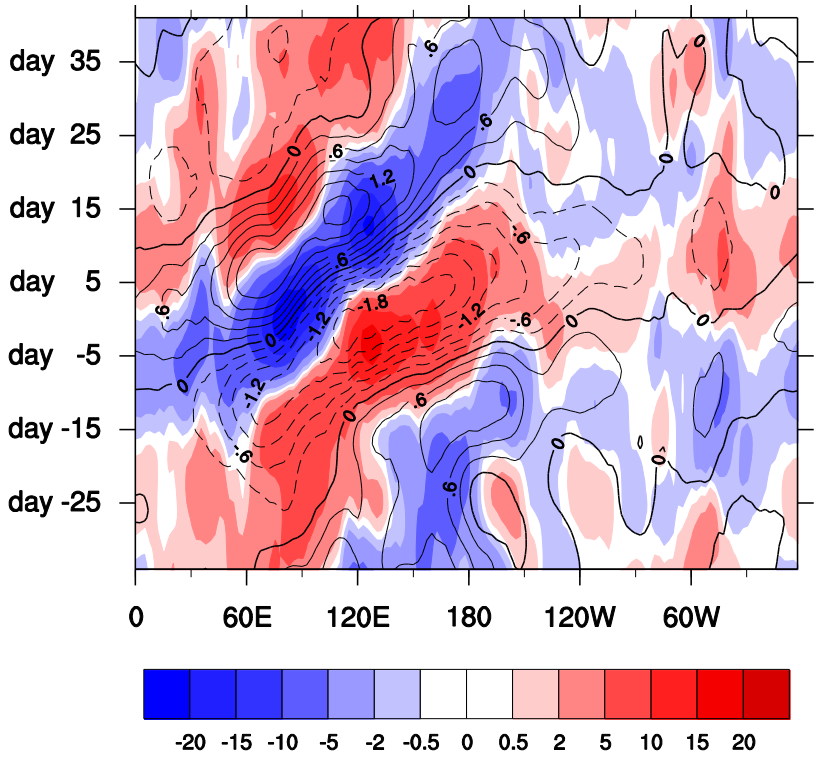

Fig. 12 Time-longitude section of the composite OLR (color; unit: Wm^{-2}) and 850hPa zonal wind (contour; unit: ms^{-1}) anomalies averaged along 20°S-0°N.

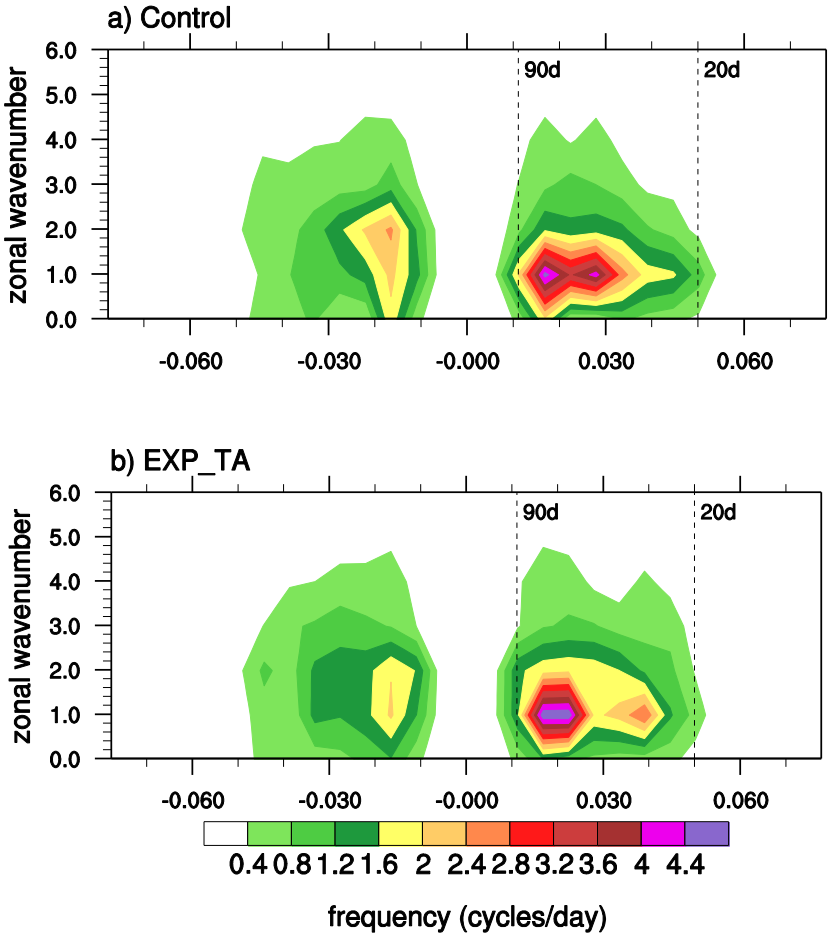

Fig. 13 The wavenumber-frequency spectra (unit: W^2m^{-4}) of the intraseasonal OLR anomaly derived from the 20-yr simulation of the Control and EXP_TA experiments. The spectrum analysis was done for a limited domain over (40°E-180°E, 20°N-20°S).

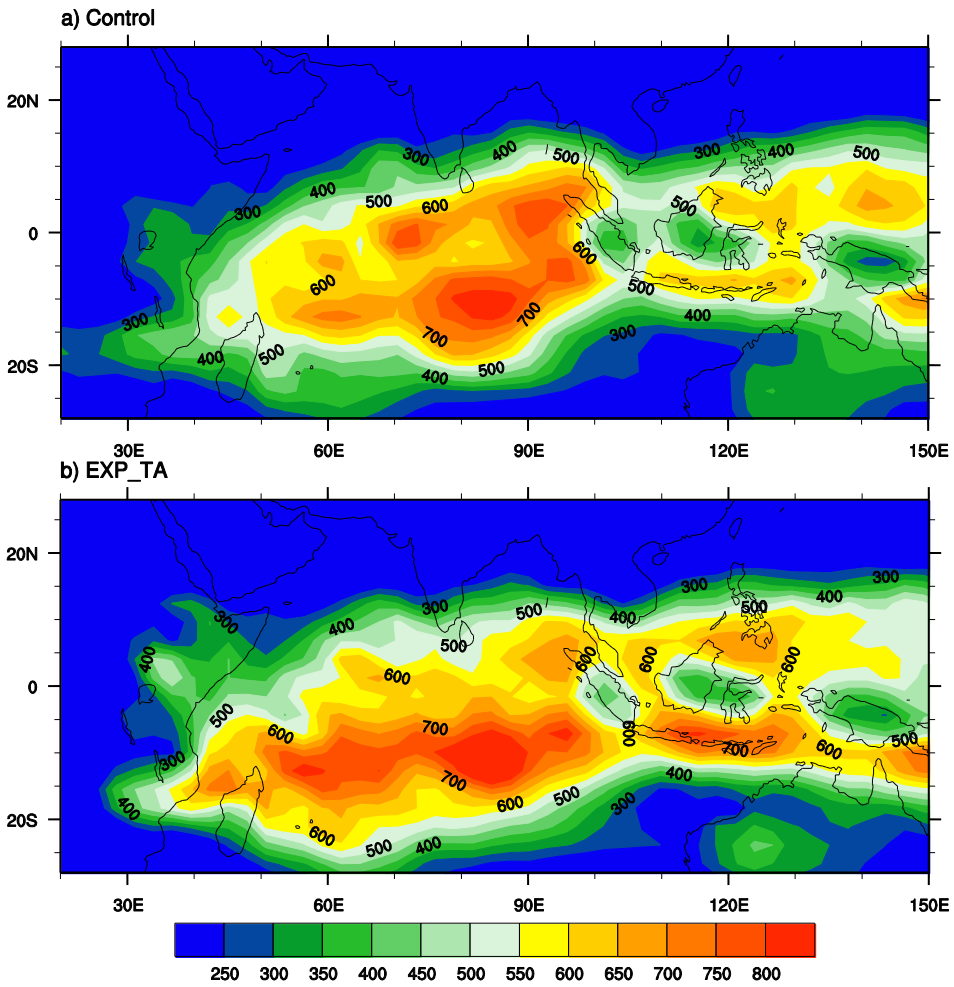

Fig. 14 Horizontal distribution of 20-90-day filtered OLR variance (unit: W^2m^{-4}) in boreal winter derived from the Control and EXP_TA experiments.

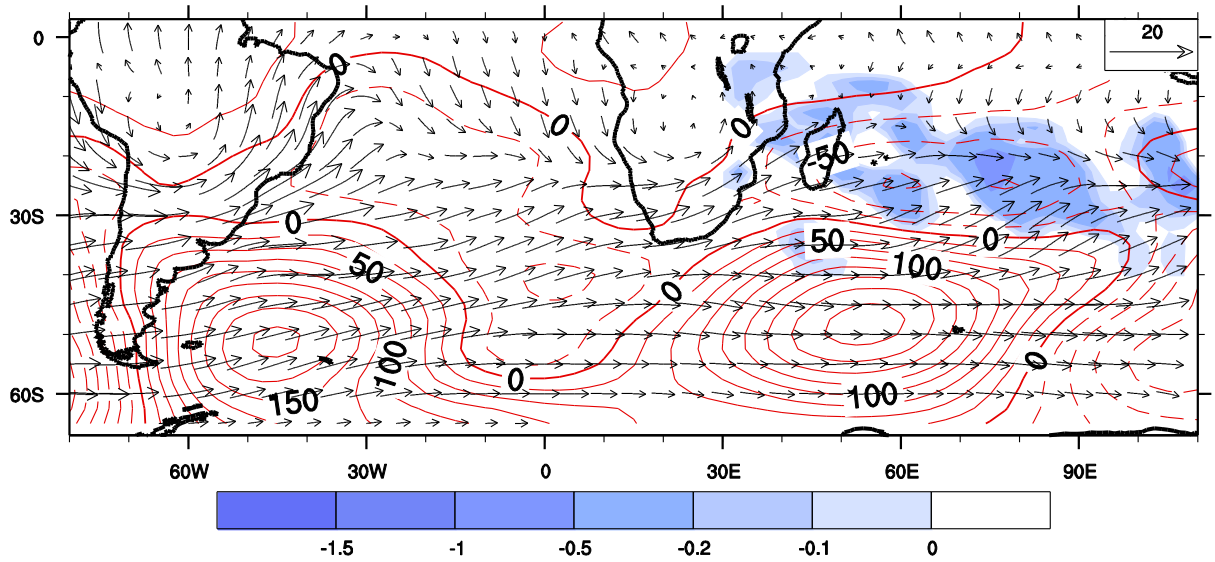

Fig. 15 20-90-day filtered observed geopotential height anomaly (contour, unit: m^2s^{-2}), Rossby wave activity flux (vector, unit: m^2s^{-2}) and wave flux divergence (color, unit: 10^{-5} ms^{-2}, only negative values are shaded over the Indian Ocean) at 200 hPa during the initiation period from day -25 to day -15.

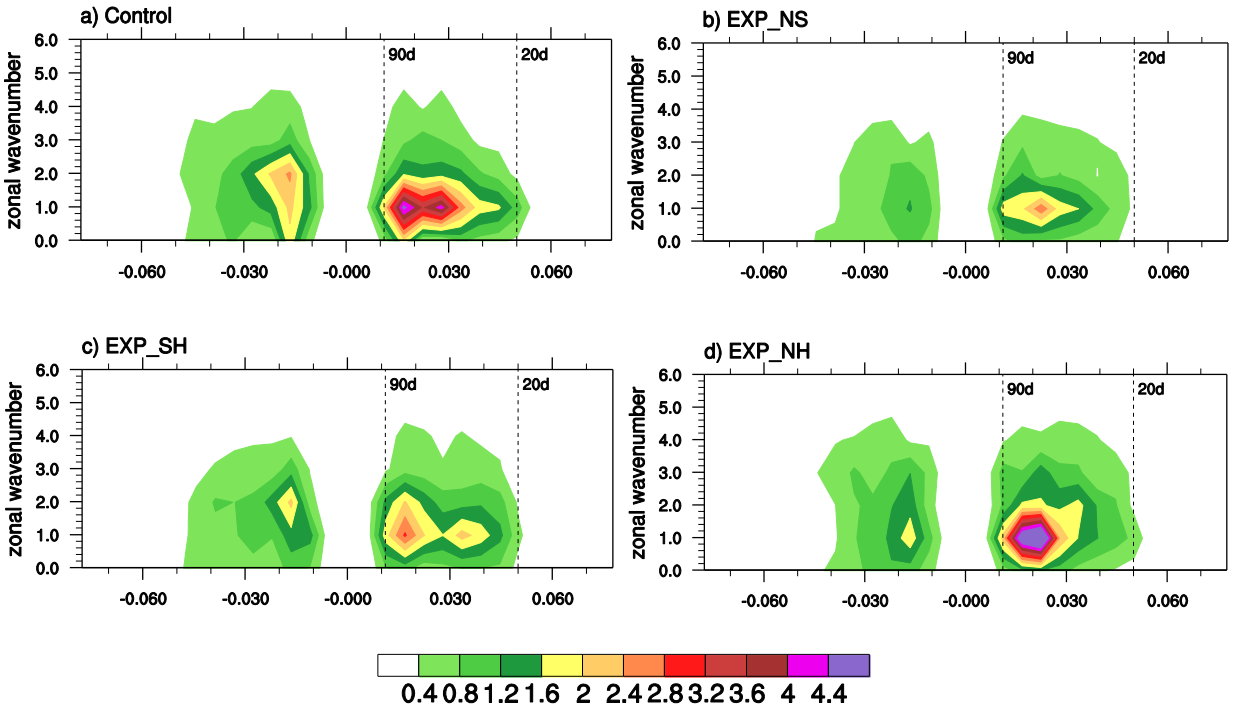

Fig. 16 Same as Fig. 13 except for the Control, EXP_NS, EXP_SH and EXP_NH experiments.

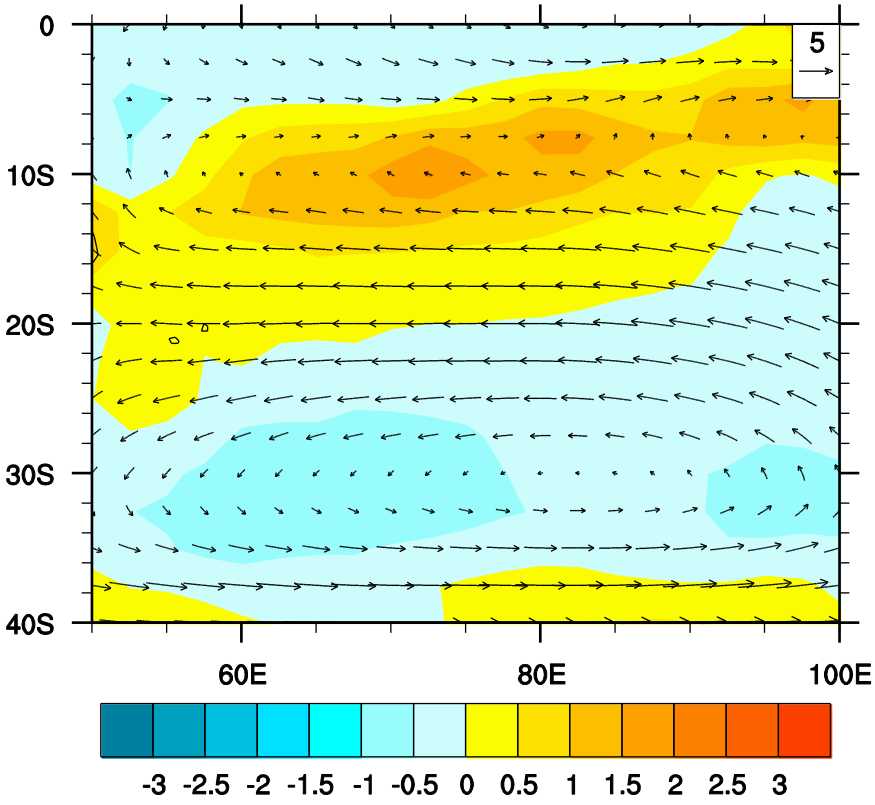

Fig. 17 Horizontal distribution of the 850-hPa barotropic energy conversion field (color, unit: 10^{-5} m^2s^{-3}) and the seasonal mean 850-hPa wind field (vector, unit: ms^{-1}).